



OPEN

Optimizing of particle accelerated rotor parameters using the discrete element method

Bo Sun^{1,2✉}, Shizhong Wei^{3,4}, Lu Yang^{3,4}, Peng Li^{1,3} & Shuaiwu Tong^{3,4}

The acceleration capability of a centrifugal jet rotor plays a crucial role in achieving a high injection velocity of powder particles in the centrifugal impact moulding process. In this regard, the focus of this article is on optimization of the runner shape. To this end, the lengths of the first and second acceleration sections (L_1 and L_2), and the angles between the first and second acceleration sections and between the second and third sections (α_1 and α_2) are considered as the rotor parameters. Simulations were conducted using multiple discrete elements to explore the influence of multiple input parameters on the response value, and a regression model was established between the parameters and the particle injection rate. The experimental results show that the selected parameters significantly affect the rate of particle injection, and the interactions between the parameters L_1 and L_2 , and between L_2 and α_2 have the largest effects. The results reveal that applying the optimized parameters improves the particle injection speed by 7.85% when compared to the pre-optimization model. This improvement in the rotor acceleration provides the basis for improving the efficiency of centrifugal impact moulding of metal powders.

Studies show that accelerated powder particles impinging on a solid-state substrate can provide a coating on the substrate surface by producing a large plastic strain deposit^{1–5}. In this technology, the velocity of the particles is the key factor in combining the particle with the substrate after impact. Currently, the common particle acceleration methods include the airflow acceleration method, mechanical acceleration method, electromagnetic acceleration method, ultrasonic acceleration method and electrostatic acceleration method. It is worth noting that each method has advantages and limitations and can be employed in various applications. In this context, the airflow acceleration method has attracted many researchers focusing on the optimization of jet structures to increase the acceleration capacity of particles. Wan⁶ studied the effect of the various parameters of the powder jet on the impact velocity and particle distribution and developed a mathematical hydrodynamic model. Gao⁷ proposed the degree of aggregation (PAD) concept and analysed the effects of the nozzle geometry on the powder flow. Cao⁸ designed the nozzle geometry based on the selected particles and propellant gases for ejected particles to reach the maximum impact velocity. Furthermore, Buhl⁹ established an analytical model, analysed the motion of the particles, and modified the nozzle structure based on CFD simulation results. Forero-Sossa¹⁰ investigated the effect of the nozzle geometry on the deposition of hydroxy-apatite particles in LPCS and demonstrated that the nozzle geometry affects the coating uniformity. Zavalan¹¹ employed an objective multi-optimization method to optimize the nozzle structure and improve nozzle performance. Klinkov¹² employed a cylindrical barrel with a double-edged bevelled exit vortex to generate a high-speed two-phase flow. This approach was suggested as an alternative to cold spray nozzles. To resolve the shortcomings of conventional DeLaval nozzles in the cold-air dynamic spraying process, Liao¹³ proposed a modified nozzle structure and verified its acceleration performance through numerical simulations. In all the aforementioned studies, it was observed that the internal structure of the flow channel exhibits a substantial influence on the acceleration effect of powder particles.

Based on the performed literature survey, the focus of present study is on investigating the mechanical acceleration of powder particles using centrifugal throw rotors. To this end, the acceleration process involving the throwing of rotors with variously shaped runners is simulated using EDEM discrete-element software. The main objective of this article is to analyse the influences of the runner control parameters on the injection velocity of

¹School of Mechatronics Engineering, Henan University of Science and Technology, Luoyang, 471003, Henan, China. ²College of Agricultural Equipment Engineering, Henan University of Science and Technology, Luoyang 471003, Henan, China. ³Joint Engineering Research Center for Abrasion Control and Moulding of Metal Materials, Henan University of Science and Technology, Luoyang 471003, Henan, China. ⁴School of Materials Science and Engineering, Henan University of Science and Technology, Luoyang 471003, Henan, China. ✉email: sunbo2020@haust.edu.cn

particles, establish a model to numerically analyse the influencing factors, and optimize the control parameters of the runner to improve the rotor acceleration performance.

Materials and methods

In this article, the discrete element method is chosen as the simulation technique. This selection is made primarily because the perturbation of the particle motion caused by the airflow is often neglected when analysing the effect of the flow channel structure on the particle acceleration performance^{14–17}. The fundamental idea behind the discrete element method is to consider the medium as a discrete body. Then the structure is discretized into independent elements and particles, where each particle is assumed to Newton's second law of motion. In this approach, the macroscopic motion of the entire medium is calculated by iteratively solving the governing equation^{18,19}. To simulate the particle motion using the discrete unitary method, vibrational equations of motion are used to model particle–particle collisions and the motion of particles at boundaries^{20,21}.

Modelling particle accelerating rotors

The rotor's internal structure of the runner consists of two elements: the runner modelling line and the section contour line, as shown in Fig. 1A, the former determines the structural characteristics of the runner and the latter determines the cross-sectional shape of the runner. The runner modelling line is composed of multi-segment lines, and the following five parameters are implemented for line control: the lengths of the first acceleration section (L_1), the lengths of the second acceleration section (L_2), the lengths of the third acceleration section (L_3), the angle between the first and second acceleration sections (α_1) and the angle between the second and third accelerating sections (α_2). These parameters, which are referred to as shape parameters, are shown in Fig. 1B. The parameter L_3 can be calculated from L_1 , L_2 , α_1 , α_2 and the known rotor radius (R) using Eq. (1). Therefore, the rotor optimization design is tested with the four key parameters L_1 , L_2 , α_1 , and α_2 in a vehicle.

$$L_3 = \sqrt{R^2 - [\sin(\alpha_1 + \alpha_2)L_1 + \sin\alpha_2L_2]^2 - \cos(\alpha_1 + \alpha_2)L_1 - \cos\alpha_2L_2} \quad (1)$$

The rotor is modelled using the SolidWorks software platform, and its internal and external structures are illustrated in Fig. 2. The parameter for the rotor are shown in Table 1, and the material properties are provided in Table 2.

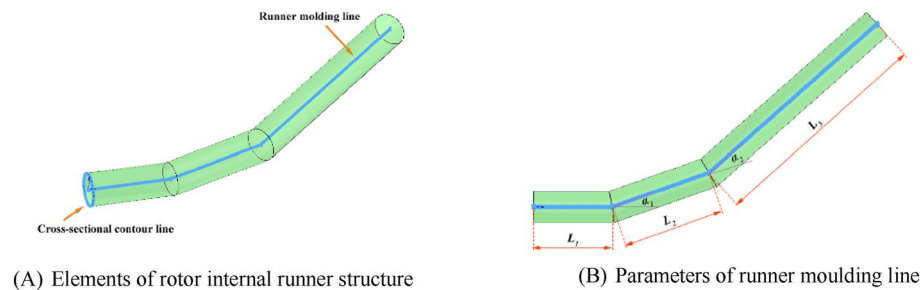


Figure 1. Rotor internal runner structure and its moulding control parameters. This figure consists of two plots. Two components of the runner inside the rotor are shown in Plot (a): the runner moulding line and the cross-section contour line. Moreover, the control parameters of the flow to the molding line are shown in Plot (b).

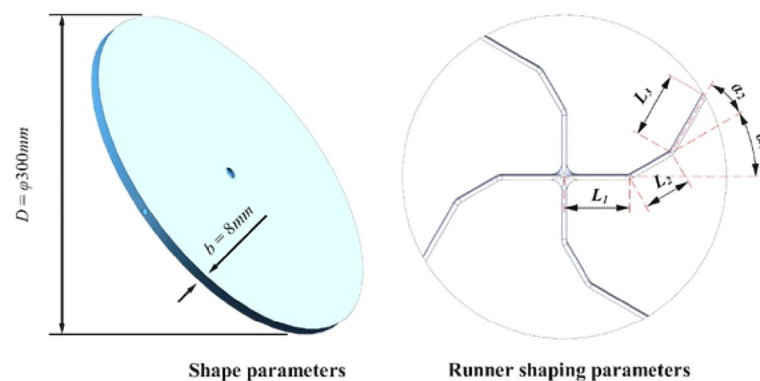


Figure 2. Rotor structure diagram. This figure shows the internal and external structure of the particle acceleration rotor.

Parameters	Value
Outer diameter of the rotor D/mm	300
Thickness of the rotor b/mm	8
Cross-sectional shape of the runner	Circle
Internal diameter of the runner section d/mm	5
Parameters of the rotor	$L_1, L_2, \alpha_1, \alpha_2$

Table 1. Table of the rotor model parameters.

Parameters	Value
Density of the material $\text{kg}\cdot\text{m}^{-3}$	7.85×10^3
Poisson's ratio of the material	0.3
Shear modulus of material MPa	2.06×10^5

Table 2. Table of rotor material parameters.

Powder particulate model

Powder particles are usually spherical with smooth surfaces. To simplify the simulation, the hard-sphere model was employed in this study. The shape parameters and material properties are provided in Table 3.

Contact pattern

Several contact models, including the Hertz–Mindlin no-slip contact model, the Hertz–Mindlin adhesion contact model, the linear adhesion contact model, the kinematic contact model at the surface, the linear elastic contact model, and the frictional loaded contact model, are commonly used²². Since the powder particles are spherical and there is no adhesion on their surfaces, the Hertz–Mindlin no-slip contact model is selected to simulate particle–particle and particle–rotor contacts. This model is schematically illustrated in Fig. 3. As shown in this figure, the contact forces between two particles fundamentally simplify into springs (with normal stiffness k_n and tangential stiffness k_t), dampers (with normal damping d_n and tangential damping d_t) and a slider (with friction coefficient μ)²³.

Parameters	Value
Radius of the particle mm	0.5
Density of the material $\text{kg}\cdot\text{m}^{-3}$	2.7×10^3
Poisson's ratio of the material	0.33
Shear modulus of the material MPa	6.89×10^3

Table 3. Pellet shape and material parameters.

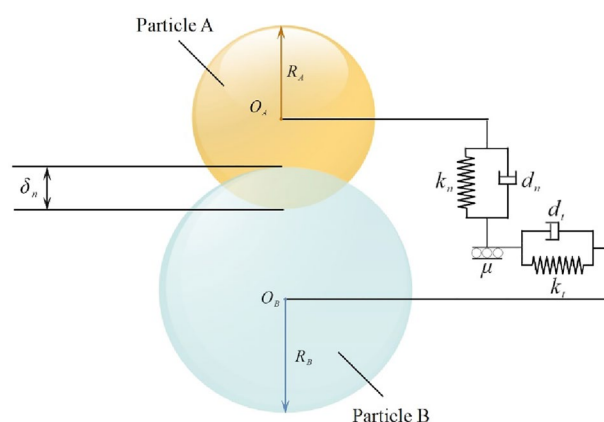


Figure 3. Hertz–Mindlin no-slip contact mechanics model. This figure illustrates the Hertz–Mindlin no-slip contact mechanics model.

In this model, the normal force between the particles, tangential force, normal damping force, and tangential damping force can be calculated using the following equations:

$$F_n = \frac{4}{3}E^*\sqrt{R^*\alpha^3} \quad (2a)$$

$$F_t = -S_t\delta \quad (2b)$$

$$F_n^d = -2\sqrt{\frac{5}{6}}\beta\sqrt{S_n m^* v_n^{rel}} \quad (2c)$$

$$\frac{1}{R^*} = \frac{1}{R_A} + \frac{1}{R_B} \quad (2d)$$

$$\frac{1}{E^*} = \frac{1 - \nu_A^2}{E_A} + \frac{1 - \nu_B^2}{E_B} \quad (2e)$$

$$\alpha = R_A + R_B - |\mathbf{r}_A - \mathbf{r}_B| \quad (2f)$$

$$S_t = 8G^*\sqrt{R^*\alpha} \quad (2g)$$

$$S_n = 2E^*\sqrt{R^*\alpha} \quad (2h)$$

$$\beta = \frac{\ln \varepsilon}{\sqrt{\ln^2 \varepsilon + \pi^2}} \quad (2i)$$

$$m^* = \frac{m_A m_B}{m_A + m_B} \quad (2j)$$

$$v_n^{rel} = (\mathbf{v}_A - \mathbf{v}_B) \cdot \mathbf{n} \quad (2k)$$

$$G^* = \frac{2 - \nu_A^2}{G_A} + \frac{2 - \nu_B^2}{G_B} \quad (2l)$$

$$\mathbf{n} = \frac{\mathbf{r}_A - \mathbf{r}_B}{|\mathbf{r}_A - \mathbf{r}_B|} \quad (2m)$$

$$T_i = -\mu_r F_n R_i \omega_i \quad (2n)$$

The parameters in the above equation are defined as follows:

E^* is the equivalent modulus of elasticity, Pa; R^* is the equivalent particle radius, m; α is the normal overlap, m; δ is the tangential overlap, m; S_t is the tangential stiffness, N/m; S_n is the normal stiffness, N/m; m^* is the equivalent mass, kg; v_n^{rel} is the normal relative velocity, m/s; v_t^{rel} is the tangential relative velocity, m/s; ν_A, ν_B is the Poisson's ratio of the particles A&B; E_A, E_B is the elastic modulus of the particle A&B, Pa; R_A, R_B is the radius of the particle A&B, m; $\mathbf{r}_A, \mathbf{r}_B$ is the spherical central position vector of the particle A&B, m; $\mathbf{v}_A, \mathbf{v}_B$ is the velocity vector of the particles A&B before collision, m/s; \mathbf{n} is the normal unit vector at the collision of the particles A&B; G^* is the equivalent shear modulus, Pa; ε is the recovery coefficient; G_A, G_B is the shear modulus of the particle A&B, Pa; μ_r is the rolling friction factor; R_i is the distance from the mass centre to the contact point, mm; ω_i is the Unit angular velocity vector of the object at the contact point, rad/s.

Simulation parameters

In the simulation, the rotor rotation speed is set to 30,000 rpm. A total of 5,000 powder particles were used in the analysis, and the simulation time was set to 0.05 s. Depending on the material of the rotor and particle, the coefficient of restitution, coefficient of static friction, and coefficient of rolling friction were selected as 0.1, 1.05, and 1.4, respectively. The Rayleigh wave method was utilized to determine the time step. Since the focus of this paper is on the launch speed and velocity of particles as they leave the rotor body, the annular grid area shown in Fig. 4 was used as the data acquisition area. In this area, is the instantaneous velocity of the particles can be determined as they are accelerated by the rotor. Figure 4 shows the configuration of the simulation model.

Box–Behnken design (BBD)

The BBD method is typically used to design response surface tests and perform an accurate statistical analysis of the test data to obtain an image with continuous features so that the mapping between the factors and the

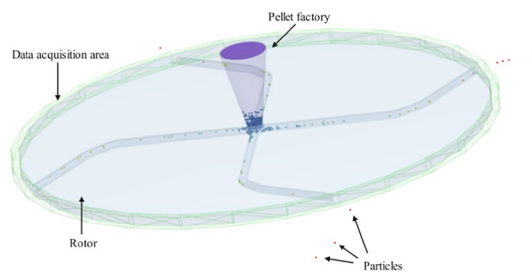


Figure 4. Simulation model. This figure illustrates the rotor-particle simulation modelling system utilized in this paper.

response values can be investigated visually²⁴. In this article, a regression model needs to be developed using the particle ejection velocity V as the target quantity and the rotor parameters L_1 , L_2 , α_1 , and α_2 as input factors. Then, the optimized design of the rotor can be achieved by solving the model. The use of the BBD response surface method allows complex unknown functional relationships between the target quantity and input factors to be fitted with simple primary or quadratic polynomial models over a small area, which is computationally easier and ensures the continuity of the predictive model. Using this method and performing ANOVA on their experimental data, this regression model can be obtained and solved for the optimal combination of parameters can be determined.

The empirical levels were determined based on the results obtained from the BBD tests shown in Table 4. Additionally, a preliminary analysis of the individual factors and a comprehensive consideration of their effects on acceleration was performed. To minimize measurement errors, each test was repeated three times and the mean values were recorded. The obtained results for each parameter level group are presented in Table 5.

Results

Based on the results of ANOVA presented in Table 6, the obtained P-value for the regression model is less than 0.0001, indicating that the regression model is highly significant. In the meantime, the obtained P-value for the model is more than 0.05, indicating that the model misfit is not significant and that the regression model fit is high. Furthermore, based on the contents of Table 7, the R^2 and adjusted R^2 values in the model are all close to one, indicating a good fit of the regression model. The predicted R^2 reasonably agrees with the adjusted R^2 , with a difference of less than 0.2. The coefficient of variation and precision are 0.25% and 27.23, respectively, indicating that the fitted regression model has a high degree of reliability.

The P-values in Table 6 for the parameters L_1 , L_2 , α_1 , and α_2 indicate that all four test factors have a highly significant effect on the injection velocity of particles. Among them, the effects of L_1 , α_1 , and α_2 are more significant compared to that of L_2 . The presented results in Table 6 obtained from the one-way ANOVA confirm that the parameters L_1 , α_1 , and α_2 significantly affect the particle injection rate, while the effect of the parameter L_2 is relatively smaller.

The parameters L_1 , L_2 , α_1 , and α_2 were selected as independent variables and denoted as x_1 , x_2 , x_3 , and x_4 , respectively. Moreover, the injection velocity of particles, denoted as V , was selected as the target variable. The least-squares method was employed to optimize the regression model. In the optimization process, four groups of single-factor first-order terms, four groups of single-factor second-order terms, and six groups of interactive-factor second-order terms were considered. Since the P-value reflects the significance of each factor in the model, when $P \leq 0.01$, the factor is considered highly significant; when $0.01 < P < 0.05$, the factor is significant; and when $P \geq 0.05$, the factor is not significant. The model can be optimized according to the P-value of each factor. Consequently, the terms BC (interaction terms for L_2 and α_1) and B^2 (the quadratic term for L_2) with $P > 0.05$ were excluded from the model. The regression model for the injection rate V can be expressed as follows:

Influence factors	Horizontal codes		
	-1	0	1
L_1 (mm)	40	65	90
L_2 (mm)	20	40	60
α_1 (°)	30	40	50
α_2 (°)	10	20	30

Table 4. Factor ranges and levels.

No	L_1 (mm)	L_2 (mm)	α_1 (°)	α_2 (°)	V (m/s)	Standard deviation
1	90	60	40	20	577.67	0.130
2	40	20	40	20	575.55	0.124
3	90	20	40	20	567.87	0.093
4	65	40	40	20	578.67	0.120
5	40	40	50	20	574.86	0.139
6	90	40	40	10	579.76	0.131
7	90	40	40	30	555.30	0.128
8	40	40	40	30	575.65	0.104
9	65	40	40	20	575.59	0.086
10	90	40	50	20	557.34	0.071
11	65	20	40	10	575.63	0.149
12	90	40	30	20	582.47	0.094
13	65	40	40	20	576.25	0.078
14	65	40	30	10	578.06	0.129
15	65	60	40	10	582.64	0.080
16	65	40	50	10	576.01	0.086
17	40	40	40	10	572.19	0.104
18	65	40	30	30	573.73	0.107
19	65	60	50	20	573.42	0.106
20	40	40	30	20	574.32	0.099
21	40	60	40	20	577.89	0.093
22	65	60	40	30	568.16	0.108
23	65	40	50	30	559.46	0.094
24	65	20	30	20	577.66	0.106
25	65	20	50	20	570.65	0.127
26	65	40	40	20	575.98	0.088
27	65	20	40	30	570.35	0.062
28	65	40	40	20	577.02	0.099
29	65	60	30	20	582.44	0.115

Table 5. BBD experimental design and results.

Source of variance	Mean square	Degrees of freedom	Sum of squares	Value of F	Value of P
Model	1274.49	14	91.03	45.41	<0.0001
A- L_1	75.25	1	75.25	37.54	<0.0001
B- L_2	50.06	1	50.06	24.97	0.0002
C- α_1	270.18	1	270.18	134.77	<0.0001
D- α_2	316.62	1	316.62	157.94	<0.0001
AB	13.91	1	13.91	6.94	0.0196
AC	164.74	1	164.74	82.17	<0.0001
AD	194.88	1	194.88	97.21	<0.0001
BC	1.01	1	1.01	0.5038	0.4895
BD	21.16	1	21.16	10.55	0.0058
CD	37.33	1	37.33	18.62	0.0007
A ²	50.39	1	50.39	25.14	0.0002
B ²	4.63	1	4.63	2.31	0.1507
C ²	16.47	1	16.47	8.22	0.0124
D ²	69.72	1	69.72	34.78	<0.0001
Residual	28.07	14	2		
Lack of fit	22.13	10	2.21	1.49	0.3729
Pure error	5.94	4	1.48		
Cor total	1302.56	28			

Table 6. Analysis of the variance for model.

Statistical indicator	Value
R2	0.9785
Adjusted R2	0.9569
Predicted R2	0.8950
Coefficient of variation (C.V.%)	0.2467
Adeq precision	27.2340

Table 7. Fit statistics.

$$\begin{aligned}
 V = & 420.22 + 1.9488x_1 + 0.0897x_2 + 3.2078x_3 + 4.3585x_4 \\
 & + 0.0037x_1x_2 - 0.0257x_1x_3 - 0.0279x_1x_4 - 0.0115x_2x_4 - 0.0306x_3x_4 \\
 & - 0.0047x_1^2 - 0.0175x_3^2 - 0.0344x_4^2
 \end{aligned} \quad (3)$$

Discussion

The influence of the runners' shape parameters on the injection rate

The effect of the individual parameters on the injection velocity

Figure 5 provides insights into the influence of individual design parameters on the injection velocity. Figure 5a depicts the effect of L_1 on the injection rate when L_2 , α_1 , and α_2 are held constant at their median values. Similarly, Fig. 5b shows the impact of L_2 on the injection rate while maintaining L_1 , α_1 , and α_2 at their median values. Figure 5c demonstrates the influence of α_1 on the injection rate with L_1 , L_2 , and α_2 set at their median values. Finally, Fig. 5d illustrates the effect of α_2 on injection velocity when L_1 , L_2 , and α_1 are held constant at their median values.

In general, the design parameters L_1 , α_1 , and α_2 exhibit a negative correlation with the injection velocity, while the parameter L_2 shows a positive correlation. The trend for each parameter can be described as follows:

- As the parameter L_1 increases from 40 to 60 mm, the injection velocity increases slightly. However, when L_1 exceeds 60 mm, the ejection velocity decreases.
- When the parameter L_2 varies in the range of 20 mm to 60 mm, there is a positive correlation between L_2 and the ejection velocity.
- When the design parameters α_1 and α_2 increase from 30 to 50 and from 10 to 30, respectively, the ejection velocity decreases.

The results reveal that L_1 , L_2 , α_1 , and α_2 affect the particle injection velocity. The optimized design involves setting the parameter L_1 around the median value (60 mm), selecting the maximal value of 60 mm for L_2 , and choosing the minimum values (30 and 10) for α_1 and α_2 , respectively. Meanwhile, it is necessary to analyse the interaction between various factors.

The influence of the multi-model parameter interactions on the injection rate

Design-Expert13 software was utilized to generate 3D response surface plots depicting the interaction effects of each shape parameter. The results align with those of the ANOVA analysis: $P_{L_1\alpha_2}(0.0001) < P_{L_1\alpha_1}(0.0001) < P_{\alpha_1\alpha_2}(0.0007) < P_{L_2\alpha_2}(0.0058) < P_{L_1L_2}(0.0196)$. The interaction between the L_1 and L_2 parameters exhibits the most substantial impact on the particle injection velocity among the various parameter interactions. Then the interaction between the parameters L_2 and α_2 has a comparatively smaller effect, while the interaction between the parameters α_1 and α_2 has a much smaller effect. Last, the interactions between the parameters L_2 and parameters α_2 and L_2 and α_2 exhibit the weakest effects. The interaction effects of the pair of parameters L_1 and L_2 , L_2 and α_2 , and α_1 and α_2 are analysed.

The interaction between the parameters L_1 (ranging from 40 to 90 mm) and L_2 (ranging from 20 to 60 mm) is illustrated in Fig. 6a, b. It is observed that as the values of L_1 increase and the values of L_2 decrease, the contour lines become along the 135 contour. This indicates a decrease in the jet velocity, which gradually transitions to an acceleration effect. Based on the distribution of the contours, the entire response surface has a maximum point of approximately 70 mm for L_1 and 50 mm for L_2 . This implies that the length of each acceleration section should be relatively constant in a multi-segment model and that the difference in length should be minimized. For example, when $L_1 = 90$ mm and $L_2 = 20$ mm, the particle jet velocity reaches its minimum value.

Figure 7a, b illustrate the interaction effect of the parameters L_2 (20 mm to 60 mm) and α_2 (10–30). It is observed that for the parameter L_2 with a value of 60 mm and α_2 with a value of 10, the peak of the entire response surface is at the top right. Furthermore, the contours gradually concentrate in the direction of the lower right-hand corner, and the degree of curvature increases gradually indicating that as the value of α_2 is increased from 30 to 10, the effect on the L_2 increases gradually. This result demonstrates that a too-large angle between the acceleration sections affects the overall acceleration effect of the rotor.

Figure 8a, b illustrate the interaction analysis of the parameters α_1 and α_2 . When the parameters α_1 and α_2 vary in the range of 30 to 40 and 10 to 20, respectively, the value of the response face has a high level of significance. The results also show a decreasing contour that thickens along 45, indicating that the particle jet velocity drops

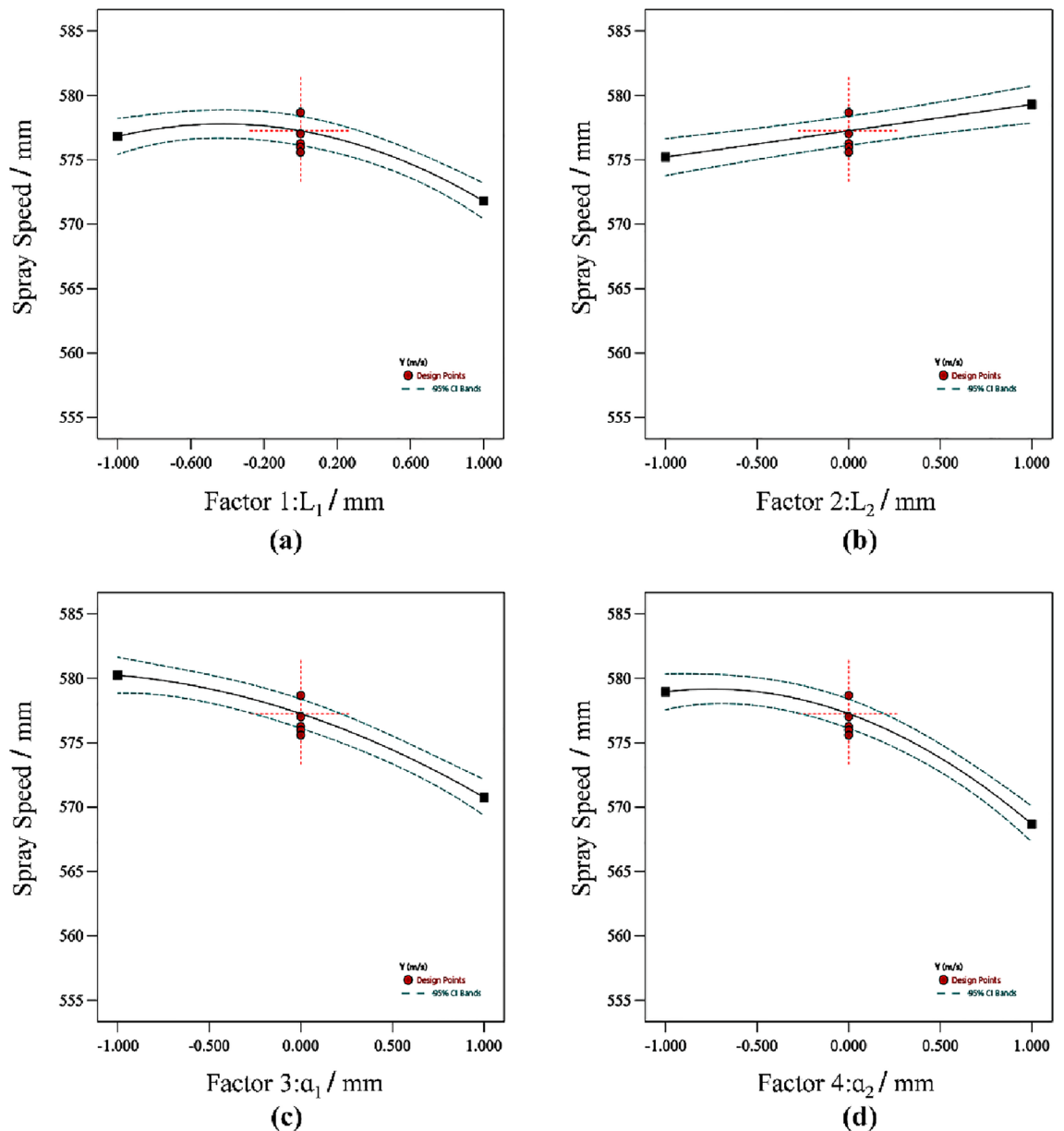


Figure 5. Effects of the individual parameters on the injection speed. This figure illustrates the influence of the multi-model parameter interactions on the injection rate. Plot (a) shows the impact of L_1 on the injection rate while maintaining L_2 , α_1 , and α_2 at their median values. Plot (b) shows the impact of L_2 on the injection rate while maintaining L_1 , α_1 , and α_2 at their median values. Plot (c) shows the impact of α_1 on the injection rate while maintaining L_1 , L_2 , and α_2 at their median values. Plot (d) shows the impact of α_2 on the injection rate while maintaining L_1 , L_2 , and α_1 at their median values.

significantly as large values are selected for the parameters α_1 and α_2 . This finding further confirms that the angle between the accelerating sections should not be too large.

Through the discussion of the independent effect of a single parameter and the interaction of multiple parameters on the spraying speed, we can conclude that the internal flow channel structure of the rotor has an important influence on the acceleration process of particles in which there exists a quantitative relationship between the structural parameters and the particle spraying speed (the acceleration capacity of the particles), which can be solved through the establishment of a mathematical model of this relationship. This change in acceleration is characterized by the acceleration process of powder particles in cold spraying^{25–29}, which can be achieved by changing the nozzle structure to increase the acceleration capacity. However, due to the lack of analysis of the overall force on the acceleration process of individual particles in the current study, it is not yet possible to completely correspond the change in the runner structure to the acceleration process of the particles, and therefore, the current acquisition of the mathematical model is still based on the statistical foundations.

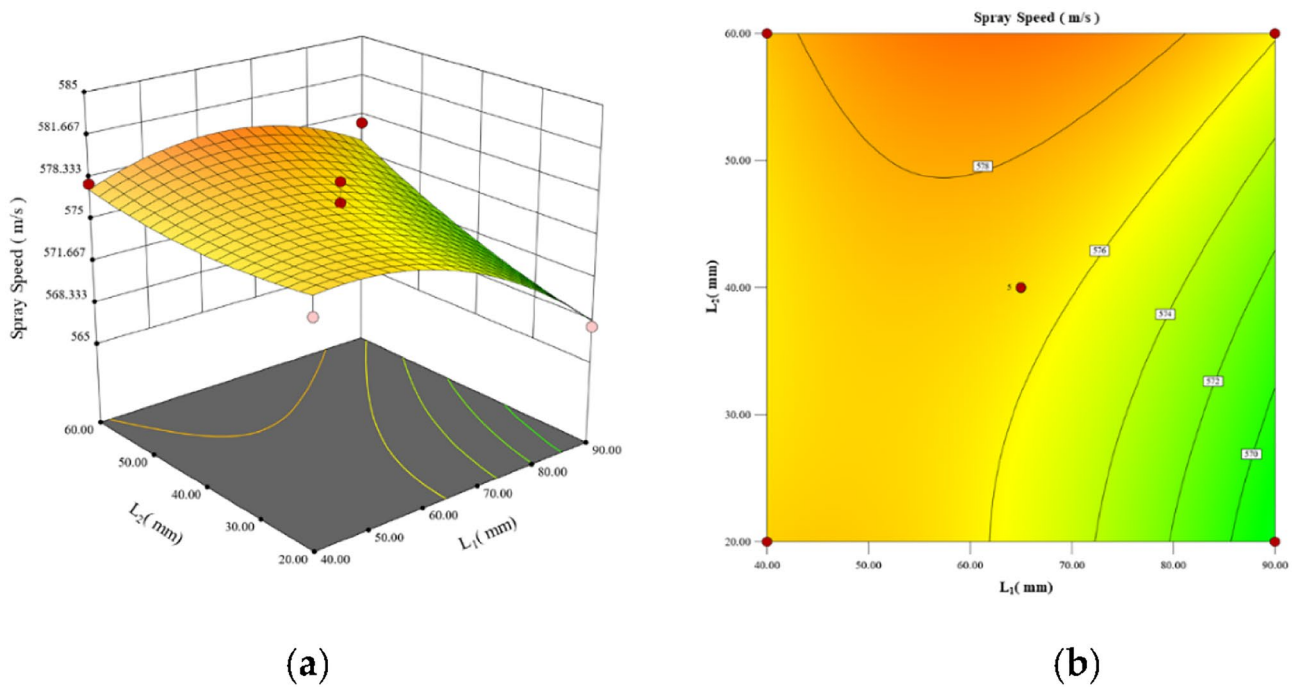


Figure 6. Mapping of the interaction effects of the parameters L_1 and L_2 . This figure consists of two pictures. Plot (a) shows the response surface of the parameters L_1 and L_2 , and Plot (b) shows the contour plots of the parameters L_1 and L_2 , both of which reflect the interaction between the two parameters.

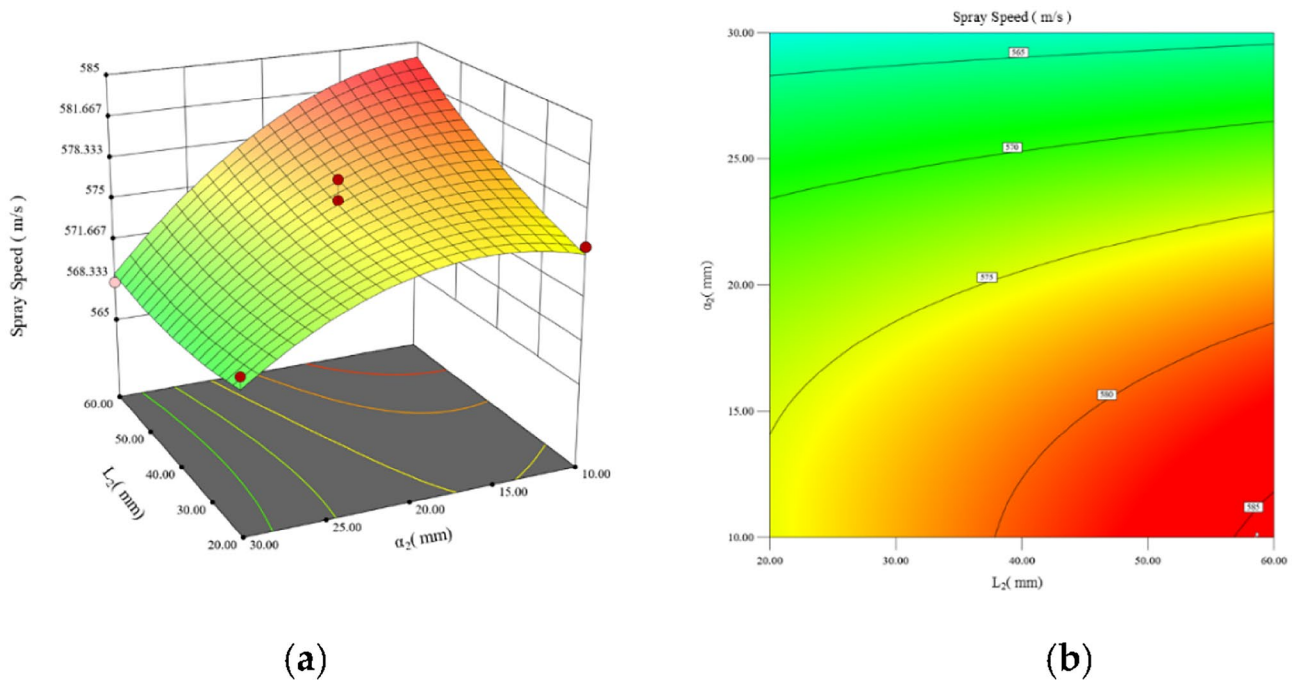


Figure 7. Mapping of the interaction effects of the parameters L_2 and α_2 . This figure consists of two plots. Plot (a) shows the response surface of the parameters L_2 and α_2 , and Plot (b) shows the contour plots of the parameters L_2 and α_2 , both of which reflect the interaction between the two parameters.

Optimum parameters and verification

Based on the solution of the regression model with the injection velocity as a condition, the optimal parameters are $L_1 = 77.37$, $L_2 = 58.67$, $\alpha_1 = 39.74$, and $\alpha_2 = 10.11$. The regression prediction of the injection velocity based on these parameters was 585.439 m/s, as illustrated in Fig. 9. Subsequently, using these optimal parameters to model the throwing rotor and conducting EDEM simulation tests, a jet speed of 587.841 was obtained, with a 0.408% error compared to the model prediction. This indicates that the established regression model can effectively

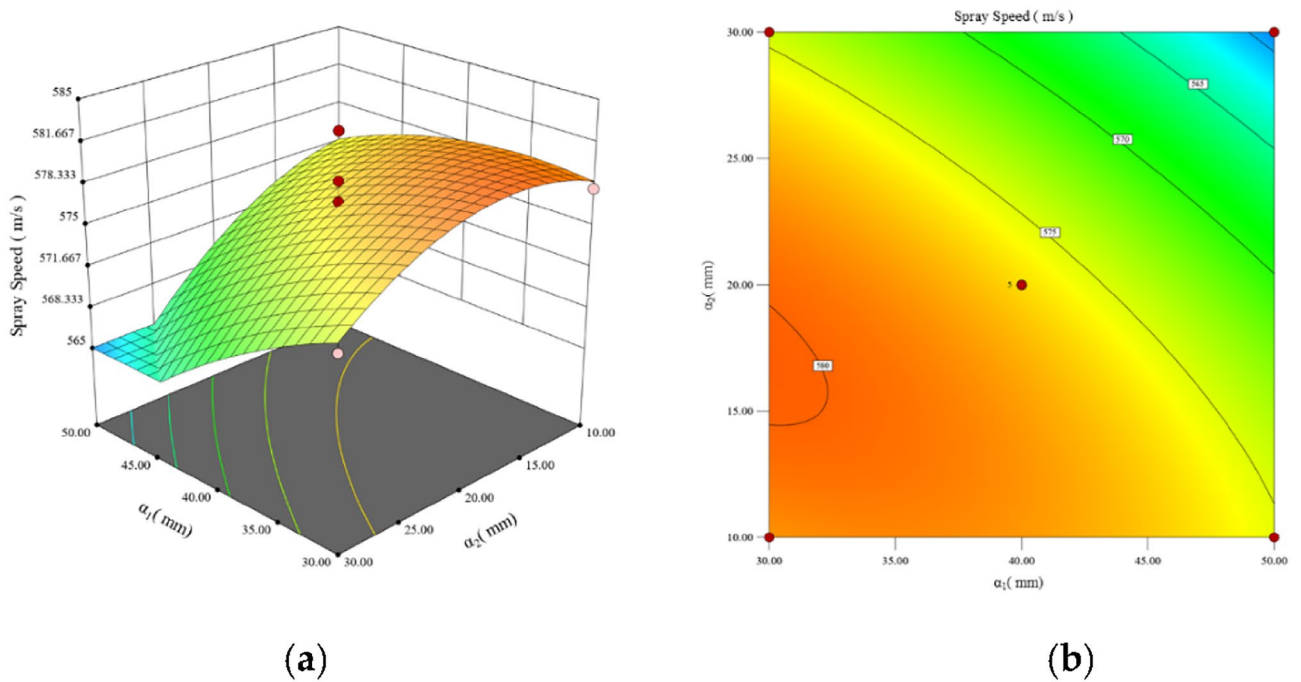


Figure 8. Mapping of the interaction effects of the parameters α_1 and α_2 . This figure consists of two plots. Plot (a) shows the response surface of the parameters α_1 and α_2 , and Plot (b) shows the contour plots of the parameters α_1 and α_2 , both of which reflect the interaction between the two parameters.

Time: 0.035 s

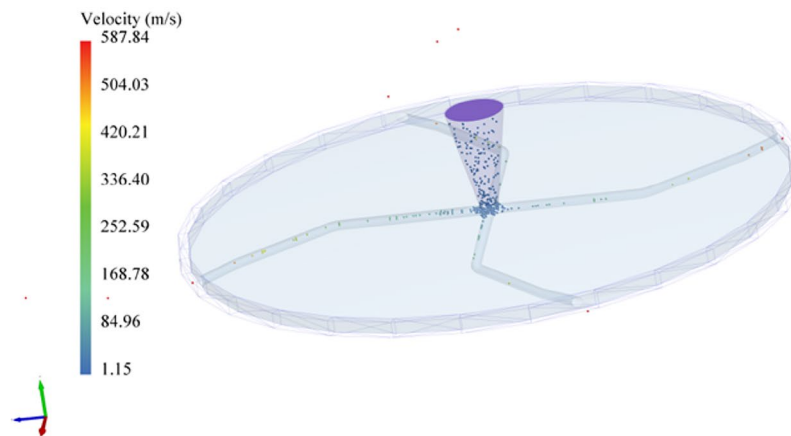


Figure 9. Acceleration of particles by the rotor after parameters optimization. This figure illustrates the acceleration of the particles by the rotor after shape parameter optimization.

predict the velocity of the particle jet based on the rotor runner parameters. Simultaneously, the EDEM simulation test of the rotor with a through-hole runner showed a particle injection speed of 545.00 m/s as illustrated in Fig. 10. By optimizing the runner design, the particle injection speed was increased by 7.85%, demonstrating that the capability of the jet rotor can be improved through runner optimization.

Conclusions

In this paper, the particle accelerating rotor was used as a research object to investigate the effect of rotor parameters on its accelerating performance. Simulations of the particle acceleration by rotors with different parameters were conducted based on the discrete cell method. In addition, the rotor acceleration performances before and after parameter optimization were compared. The main conclusions can be summarized as follows.

Time: 0.035 s

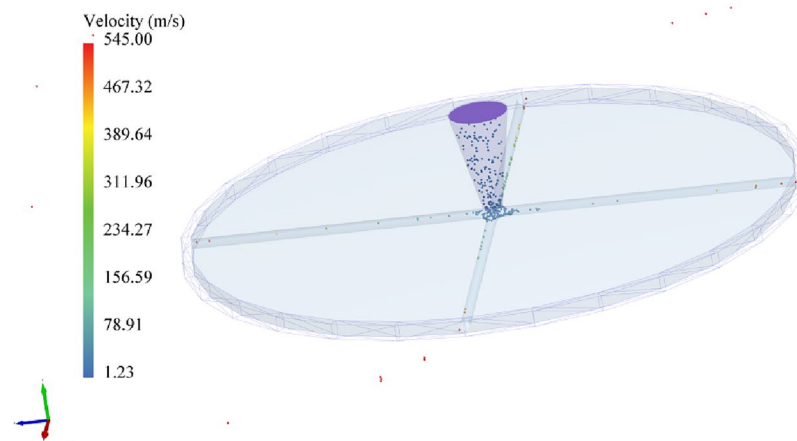


Figure 10. Acceleration of particles by the rotor with a through-hole runner. This figure illustrates the acceleration of the particles by the rotor with a through-hole runner.

- (1) In this study, the accelerated rotor is modelled using SolidWorks and its acceleration performance is simulated using EDEM. By analysing the simulation results of 25 groups of rotors, a multivariate nonlinear regression model is established for the first time based on rotor parameters.
- (2) By analysing the regression model, it is proven that all four modelling parameters have significant effects on the particle ejection velocity. It was found that L_1 , α_1 , and α_2 are negatively correlated with the injection speed, while L_2 exhibits a positive correlation. The interaction between L_1 and L_2 had the largest effect, followed by the interaction between L_2 and α_2 , whereas the interaction between α_1 and α_2 had a smaller effect, and the interaction of the other factors was not significant.
- (3) The accelerating rotor parameters were optimized using a regression model for parametric optimization. By analysing the simulation results, the improvement in the rotor acceleration capacity before and after optimization is 7.85%.

The results show that the optimization of the rotor parameters can enhance the acceleration capacity for particles, which provides a feasible solution for improving the quality and efficiency of the centrifugal impact caused by metal powders. However, further improvement of this forming method requires in-depth studies of more complex rotor structures and forming environmental conditions, as well as the optimization of the forming process control strategies.

Data availability

The datasets generated during and/or analysed during the current study are available from the corresponding author upon reasonable request.

Received: 4 August 2023; Accepted: 31 October 2023

Published online: 01 November 2023

References

1. Raelison, R. N. *et al.* Cold gas dynamic spray technology: A comprehensive review of processing conditions for various technological developments till to date. *Addit. Manuf.* **19**, 134–159. <https://doi.org/10.1016/j.addma.2017.07.001> (2018).
2. Yin, S., Meyer, M., Li, W., Liao, H. & Lupoi, R. Gas flow, particle acceleration, and heat transfer in cold spray: A review. *J. Therm. Spray Technol.* **25**, 874–896. <https://doi.org/10.1007/s11666-016-0406-8> (2016).
3. Aadaan-Nyiaik, M. A. & Tiamiyu, A. A. Recent advances on bonding mechanism in cold spray process: A review of single-particle impact methods. *J. Mater. Res.* **38**, 69–95. <https://doi.org/10.1557/s43578-022-00764-2> (2023).
4. Irissou, E., Legoux, J.-G., Ryabinin, A. N., Jodoin, B. & Moreau, C. Review on cold spray process and technology: Part I—intellectual property. *J. Thermal Spray Technol.* **17**, 495–516. <https://doi.org/10.1007/s11666-008-9203-3> (2008).
5. Singh, S.K., Chattopadhyaya, S., Murtaza, Q., Pandey, S.M., Walia, R.S., Tyagi, M. & Kumar, S. A comprehensive review of cold spray coating technique. In *Proceedings of the Recent Trends in Mechanical Engineering, Singapore, 2023*. 175–181 (2023).
6. Wan, W., Li, W., Wu, D., Qi, Z. & Zhang, Z. New insights into the effects of powder injector inner diameter and overhang length on particle accelerating behavior in cold spray additive manufacturing by numerical simulation. *Surf. Coat. Technol.* **2022**, 444. <https://doi.org/10.1016/j.surfcoat.2022.128670> (2022).
7. Gao, X., Yao, X. X., Niu, F. Y. & Zhang, Z. The influence of nozzle geometry on powder flow behaviors in directed energy deposition additive manufacturing. *Adv. Powder Technol.* **2022**, 33. <https://doi.org/10.1016/j.apt.2022.103487> (2022).
8. Cao, C. *et al.* The associated effect of powder carrier gas and powder characteristics on the optimal design of the cold spray nozzle. *Surf. Eng.* **36**, 1081–1089. <https://doi.org/10.1080/02670844.2020.1744297> (2020).
9. Buhl, S., Breuninger, P. & Antonyuk, S. Optimization of a laval nozzle for energy-efficient cold spraying of microparticles. *Mater. Manuf. Process.* **33**, 115–122. <https://doi.org/10.1080/10426914.2017.1279322> (2018).

10. Andrea Forero-Sossa, P. *et al.* Nozzle geometry and particle size influence on the behavior of low pressure cold sprayed hydroxyapatite particles. *Coatings* <https://doi.org/10.3390/coatings12121845> (2022).
11. Zavalan, F.-L. & Rona, A. A workflow for designing contoured axisymmetric nozzles for enhancing additively manufactured cold spray deposits. *Addit. Manuf.* <https://doi.org/10.1016/j.addma.2022.103379> (2023).
12. Klinkov, S. V., Kosarev, V. F. & Zaikovskii, V. N. Influence of flow swirling and exit shape of barrel nozzle on cold spraying. *J. Therm. Spray Technol.* **20**, 837–844. <https://doi.org/10.1007/s11666-011-9621-5> (2011).
13. Liao, Q. & Tan, Z. Numerical investigations of cold gas dynamic spray with a novel convergent-divergent nozzle. In *Proceedings of the 11th International Conference of Numerical Analysis and Applied Mathematics (ICNAAM), Greece, 2013 Sep 21–27, 2013*. 2333–2336 (2013).
14. Duan, D.R., Wang, S., Zhao, F. & Su, D.N. Analysis of particle motion in vertical shaft impact crusher rotor. In *Proceedings of the 2nd International Conference on Manufacturing Science and Engineering, Guilin, People's Republic of China, 2011 Apr 09–11, 2011*. 54–57 (2011).
15. Feng, F., Shi, J., Yang, J. & Ma, J. Correlation between the angle of the guide plate and crushing performance in vertical shaft crushers. *Shock Vib.* <https://doi.org/10.1155/2022/9991855> (2022).
16. Guo, W., Zhao, F. & Li, S. The discussion of rotor guide channel length of vertical shaft impact crushing test machine. In *Proceedings of the International Conference on Materials Science, Machinery and Energy Engineering (MSMEE 2013), Hong Kong, Peoples Republic of China, 2014 Dec 24–25, 2013*. 494–499 (2013).
17. Wang, S., Zhao, F. & Duan, D. Research of vertical shaft impact crusher rotor channels' number based on EDEM. *Proc. Int. Conf. Mech. Indus. Manuf. Eng. Melbourne Australia* **15–16**(2011), 253–256 (2011).
18. Cundall, P. A. & Strack, O. D. L. A discrete numerical model for granular assemblies. *Geotechnique* **29**, 47–65. <https://doi.org/10.1680/geot.1979.29.1.47> (1979).
19. Thornton, C. *Granular Dynamics, Contact Mechanics and Particle System Simulations* (Springer, 2021).
20. Modeling and simulation. In *Understanding the Discrete Element Method*. 213–221 (2014).
21. Zhu, H. P., Zhou, Z. Y., Yang, R. Y. & Yu, A. B. Discrete particle simulation of particulate systems: A review of major applications and findings. *Chem. Eng. Sci.* **63**, 5728–5770. <https://doi.org/10.1016/j.ces.2008.08.006> (2008).
22. Popp, A. & Wriggers, P. *Contact Modeling for Solids and Particles* (Springer, 2018).
23. Di Renzo, A. & Di Maio, F. P. Comparison of contact-force models for the simulation of collisions in DEM-based granular flow codes. *Chem. Eng. Sci.* **59**, 525–541 (2004).
24. Kayaroganam, P. *Response Surface Methodology in Engineering Science* (IntechOpen, 2021).
25. Klinkov, S., Kosarev, V., Shikalov, V. & Vidyuk, T. Development of ejector nozzle for high-pressure cold spray application: A case study on copper coatings. *Int. J. Adv. Manuf. Technol.* **125**, 4321–4328. <https://doi.org/10.1007/s00170-023-11047-3> (2023).
26. Zavalan, F.-L. & Rona, A. A workflow for designing contoured axisymmetric nozzles for enhancing additively manufactured cold spray deposits. *Add. Manuf.* **62**, 103379. <https://doi.org/10.1016/j.addma.2022.103379> (2023).
27. Forero-Sossa, P. A. *et al.* Nozzle geometry and particle size influence on the behavior of low pressure cold sprayed hydroxyapatite particles. *Coatings* <https://doi.org/10.3390/coatings12121845> (2022).
28. Garmeh, S., Jadidi, M., Lamarre, J.-M. & Dolatabadi, A. Cold spray gas flow dynamics for on and off-axis nozzle/substrate hole geometries. *J. Therm. Spray Technol.* **32**, 208–225. <https://doi.org/10.1007/s11666-022-01487-w> (2023).
29. Bernard, C. A., Takana, H., Lame, O., Ogawa, K. & Cavaillé, J. Y. Influence of the nozzle inner geometry on the particle history during cold spray process. *J. Therm. Spray Technol.* **31**, 1776–1791. <https://doi.org/10.1007/s11666-022-01407-y> (2022).

Author contributions

B.S. wrote the main manuscript text. Shizhong Wei reviewed and edited the manuscript. L.Y. prepared Figs. 1, 2, 3, 4, 5, 6, 7, 8, 9 and 10. P.L. and S.T. assisted in completing the simulation experiments. All authors reviewed the manuscript.

Funding

This work was financially supported by the National Key R&D Program of China (2020YFB2008400).

Competing interests

The authors declare no competing interests.

Additional information

Correspondence and requests for materials should be addressed to B.S.

Reprints and permissions information is available at www.nature.com/reprints.

Publisher's note Springer Nature remains neutral with regard to jurisdictional claims in published maps and institutional affiliations.



Open Access This article is licensed under a Creative Commons Attribution 4.0 International License, which permits use, sharing, adaptation, distribution and reproduction in any medium or format, as long as you give appropriate credit to the original author(s) and the source, provide a link to the Creative Commons licence, and indicate if changes were made. The images or other third party material in this article are included in the article's Creative Commons licence, unless indicated otherwise in a credit line to the material. If material is not included in the article's Creative Commons licence and your intended use is not permitted by statutory regulation or exceeds the permitted use, you will need to obtain permission directly from the copyright holder. To view a copy of this licence, visit <http://creativecommons.org/licenses/by/4.0/>.

© The Author(s) 2023